International Journal of Thermophysics, Vol. 27, No. 5, September 2006 (© 2006)
DOI: 10.1007/s10765-006-0109-3

Numerical Simulation of Natural Convection Flow Over Parabolic Bodies[1]

O. M. Haddad[2,3] and A. Bany-Youness[2]

Received October 24, 2005

Steady, two-dimensional and symmetric natural convection flow over parabolic bodies are investigated numerically. The full Navier–Stokes and energy equations were solved using the finite element technique. Solutions for the velocity and temperature distributions are obtained for different values of the flow parameters. In addition, the local and average Nusselt number distributions are obtained and presented. For all cases considered, the following parameters are studied: nose radius of curvature of the parabolic body, Grashof number, and Prandtl number. It was found that as the nose radius of curvature of the parabolic body is increased, the local and average values of the Nusselt number are decreased. On the other hand, an increase in the Grashof or Prandtl number is found to increase the local and average Nusselt number.

KEY WORDS: natural convection; numerical simulation; parabolic body.

1. INTRODUCTION

The importance of flow over parabolic bodies comes from the fact that the flow over a semi-infinite flat plate is fundamental in engineering applications. However, flat plates considered by most researchers in the literature are infinitesimally thick (e.g., see Davis [1]). In real-life applications, all bodies have finite thickness, including the flat plate. Thus, the flow over a parabolic body represents the flow over a flat plate more closely, with

[1] This paper is dedicated to A. Bany-Youness. He passed away in 2003 and the components of this paper have been collected from his M.Sc. thesis work after his death.

[2] Department of Mechanical Engineering, Jordan University of Science and Technology, P.O. Box 3030, Irbid 22110, Jordan.

[3] To whom correspondence should be addressed. E-mail: haddad@just.edu.jo

the effect of a blunt leading edge being implicitly considered if the leading edge region is not excluded from the solution.

Davis [1] has studied the laminar flow past a semi-infinite flat plate. In his study, Davis used a series truncation method in which the stream function is locally expanded in a power series in the x-coordinate. Van De Vooren and Dijkstra [2] have investigated the laminar incompressible flow past a semi-infinite flat plate, and a numerical solution to the Navier–Stokes (N–S) equations has been reached.

The flow over a parabolic body is the natural extension of the flow over a flat plate when parabolic coordinates are used. The N–S equations for laminar incompressible flow past a parabolic cylinder were numerically solved by Botta et al. [3]. The same flow problem that is investigated by Davis [1] was treated also by Dennis and Walsh [4] using the finite difference technique. The stream function and vorticity variables are used as the dependent variables. In their study, they were not able to get a solution for a Reynolds number smaller than 0.25. This was because of the singularity problem; however, their results were in good agreement with those of Davis [1]. There was a small but significant difference between their results and those of the second-order boundary layer approximation, especially in the skin friction. Davis [5] has numerically solved the laminar incompressible flow past a parabolic cylinder for a wide range of Reynolds numbers. All solutions were found by using an alternating direction implicit (ADI) method. Davis paid careful attention on extracting the singularities from the problem in the limit as the Reynolds number goes to zero (i.e., infinitesimal flat-plate solution). In addition, Haddad and Corke [6] have investigated the receptivity of the boundary layer over parabolic bodies to a free-stream acoustic wave. The flow over a parabolic body was one part (the basic state) of the solution.

All past solutions of the flow over a parabolic body have considered only the hydrodynamic part of the problem. The only exception to this is the numerical study carried out by Haddad et al. [7], in which the full Navier–Stokes and forced convection energy equations in parabolic coordinates with the stream function, vorticity and temperature as dependent variables were solved. Results were presented for the pressure, velocity, and temperature distributions in addition to the local and average skin friction distributions. The effect of both the Reynolds number and Prandtl number on the local and average Nusselt number was also presented. The obtained solutions agreed very well with the previous solutions available in the literature.

The goal of this study is to extend our previous work reviewed above to the case of natural convection flow over parabolic bodies. The effect of the different flow parameters (e.g., nose radius of curvature, Prandtl

number, etc.) will be investigated. Furthermore, Nusselt number distributions will be obtained, and all results relevant to the parabolic body will be compared with the classical flat plate results in an attempt to understand the effect of bluntness of the leading edge.

To the best of authors' knowledge, there exist no experimental data in the literature relevant to the flow over parabolic bodies, nor a theoretical or numerical study which considers the natural convection flow over parabolic bodies. This lack of knowledge in the literature, in addition to the wide practical applications of the flow over finite thickness flat plates, have motivated the present study.

2. MATHEMATICAL FORMULATION OF THE PROBLEM

2.1. Governing Equations

A schematic diagram of the problem under consideration is shown in Fig. 1. The surface of the parabolic body is generated based on the following equation:

$$x(y) = \frac{1}{2R}\left(y^2 - R^2\right), \tag{1}$$

where R is recognized as the nose radius of curvature.

The full Navier–Stokes and energy equations for steady two-dimensional laminar incompressible flow in the Cartesian coordinates take the form [7],
Continuity equation:

$$\frac{\partial u^*}{\partial x^*} + \frac{\partial v^*}{\partial y^*} = 0 \tag{2}$$

x-momentum equation:

$$\rho u^* \frac{\partial u^*}{\partial x^*} + \rho v^* \frac{\partial u^*}{\partial y^*} = \rho g_x - \frac{\partial P^*}{\partial x^*} + \mu\left[\frac{\partial^2 u^*}{\partial x^{*2}} + \frac{\partial^2 u^*}{\partial y^{*2}}\right], \tag{3}$$

where $g_x = -g$.
y-momentum equation:

$$\rho u^* \frac{\partial v^*}{\partial x^*} + \rho v^* \frac{\partial v^*}{\partial y^*} = -\frac{\partial P^*}{\partial y^*} + \mu\left[\frac{\partial^2 v^*}{\partial x^{*2}} + \frac{\partial^2 v^*}{\partial y^{*2}}\right] \tag{4}$$

Energy equation:

$$u^* \frac{\partial T^*}{\partial x^*} + v^* \frac{\partial T^*}{\partial y^*} = \alpha\left(\frac{\partial^2 T^*}{\partial x^{*2}} + \frac{\partial^2 T^*}{\partial y^{*2}}\right). \tag{5}$$

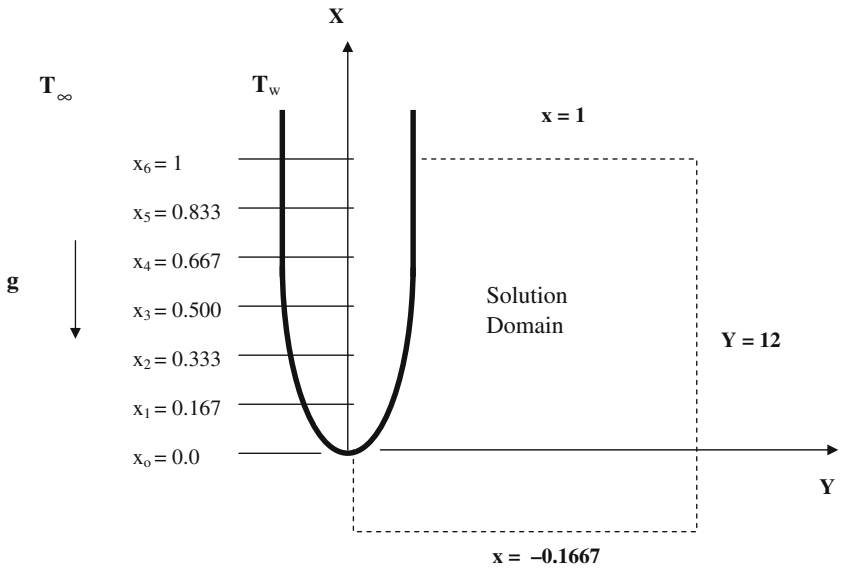

Fig. 1. Schematic diagram of physical problem.

It is assumed that there is no heat source/sink, that the thermophysical properties are constant, and that the viscous dissipation is negligible. In order to make the equations dimensionless, the following dimensionless variables are introduced:

$$x = \frac{x^*}{L}, \quad y = \frac{y^*}{L}, \quad u = \frac{u^*}{\upsilon/L}, \quad v = \frac{v^*}{\upsilon/L}$$
$$\theta = \frac{T^* - T^*_\infty}{T^*_w - T^*_\infty} \quad , \quad P = \frac{P^* - P^*_\infty}{\rho\upsilon^2/L^2} \tag{6}$$

Substituting these variables back into Eqs. (2)–(5), and using the Boussinesq approximation, leads to the following dimensionless set of equations: Continuity equation :

$$\frac{\partial u}{\partial x} + \frac{\partial v}{\partial y} = 0 \tag{7}$$

x-momentum equation:

$$u\frac{\partial u}{\partial x} + v\frac{\partial u}{\partial y} = \mathrm{Gr_L}\,\theta + \frac{\partial^2 u}{\partial x^2} + \frac{\partial^2 u}{\partial y^2} \tag{8}$$

y-momentum equation:

$$u\frac{\partial v}{\partial x}+v\frac{\partial v}{\partial y}=\frac{\partial^2 v}{\partial x^2}+\frac{\partial^2 v}{\partial y^2} \tag{9}$$

Energy equation :

$$u\frac{\partial \theta}{\partial x}+v\frac{\partial \theta}{\partial y}=\frac{1}{\mathrm{Pr}}\left(\frac{\partial^2 \theta}{\partial x^2}+\frac{\partial^2 \theta}{\partial y^2}\right), \tag{10}$$

where Gr is the Grashof number and Pr is the Prantdl number.

2.2. Local and Average Nusselt Number

The local Nusselt number is defined as

$$\mathrm{Nu}_x=\frac{h x^*}{k}, \tag{11}$$

where h is the convection heat transfer coefficient and is given by

$$h=\frac{-k(\partial T^*/\partial y^*)_{\mathrm{w}}}{\Delta T^*}, \tag{12}$$

where $\Delta T^*=T_{\mathrm{w}}^*-T_{\infty}^*$

Thus, by making the variables dimensionless using Eq. (6),

$$\mathrm{Nu}_x=-x\left(\frac{\partial \theta}{\partial y}\right)_{\mathrm{w}}. \tag{13}$$

This equation indicates that the local Nusselt number is directly proportional to the gradient of the local dimensionless temperature profile at the wall. The average Nusselt number may then be calculated as follows:

$$\overline{\mathrm{Nu}}=\frac{1}{L}\int_0^L \mathrm{Nu}_x\,\mathrm{d}x. \tag{14}$$

2.3. Boundary Conditions

Since the x-axis is an axis of symmetry (Fig. 1), only one half of the flow domain will be considered. At the wall, the no-slip no-penetration conditions ($u = 0,\ v = 0$) are applied, whereas the wall temperature was considered constant ($T = T_w$). Away from the wall in the y-direction, the ambient conditions are imposed. The above boundary conditions can be summarized as follows:

– *Wall boundary conditions* ($y = y_w, x_o < x < x_6$):

$$u = 0, v = 0, \text{ and } \theta = 1.0. \tag{15}$$

– *Free-stream boundary conditions* ($y \to \infty$):

$$u = 0, v = 0, \text{ and } \theta = 0. \tag{16}$$

– *Symmetry boundary condition* ($y = 0,\ x < x_o$):

$$v = 0. \tag{17}$$

In addition, the following boundary conditions are required to close the computational domain:

– Inflow conditions at $x = -0.1667$: $\theta = 0$. (18)

– Outflow conditions at $x = x_6$: all velocity components have zero gradients at the outflow

$$\partial u/\partial x = \partial v/\partial x = 0. \tag{19}$$

3. NUMERICAL METHOD OF SOLUTION

The governing set of partial differential equations and boundary conditions has been solved using the finite element technique. The numerical algorithm follows the "SIMPLER" algorithm introduced by Patankar [8]. The numerical tests were performed using two different types of elements: quadratic and cubic triangular elements. Here, it should be emphasized that the accuracy of the solution was improved by using higher-order elements (i.e., triangular elements). The results were verified using a mesh refinement approach in which the total number of node points is continuously increased as long as the numerical solution is changing, and until the numerical solution is invariant with any further increase in the total

number of node points. This mesh refinement approach was repeated for all cases considered. The results presented here were obtained using third-order triangular elements, with a total number of elements and nodes of 508 and 1077, respectively. The resulting set of algebraic equations is non-linear, and thus iterative methods are required. Picard's method or sometimes called the successive substitution method (Anderson et al. [9]) was used. In this method an initial estimate of the solution variables (u, v, θ) are substituted in the governing equations. The equations are solved for new values that are then used as the estimates for the next iteration.

The program will continue iteratively until the convergence criterion is achieved. The convergence criterion is the level at which the specified variable's residual norm is reached. For each of the variables, there will be an equation for each finite element node in the analysis model. A typical algebraic equation for variable ϕ at node i can be written as

$$A_{ii}\phi_i + \sum_{j \neq i} A_{ij}\phi_j = S_{ti}, \tag{20}$$

where A_{ij}'s are the algebraic coefficients resulting from discretizing the advection and diffusion terms in the governing equations, and S_{ti}'s are the discretized source terms.

The residual of this equation is defined as

$$R_{\phi i} = S_{ti} - A_{ii}\phi_i - \sum_{j \neq i} A_{ij}\phi_j, \tag{21}$$

where $R_{\phi i}$ is the nodal residual for ϕ at node i. Solutions were assumed to converge when $R_{\phi i} \leq 10^{-5}$ is satisfied for every dependent variable ϕ at every node point i in the computational domain.

In order to slow down the changes made to the solution variables, an under-relaxation technique was used. In this method, the new solution is weighted by the old solution using the following formula:

$$\phi = \gamma\phi_{\text{new}} + (1-\gamma)\phi_{\text{old}}. \tag{22}$$

for most situations, the value $\gamma = 0.5$ was the best choice.

4. RESULTS AND DISCUSSION

To validate our results, the solution for a nose radius $r = 0$ (i.e., zero-thickness flat plate) case is obtained. Also, the case for $r = 0.01$ (i.e., parabolic body) was considered to check the code capability under forced-flow conditions. The results of these two cases are then compared

with pertinent available results in the literature. Other cases of natural convection flow for which $r = 0.001$, 0.01, 0.1 are then considered to investigate the effect of the parameters of interest on the solution.

4.1. Validation of Results

When the nose radius of curvature takes the value zero, the parabolic body becomes a zero-thickness flat plate. Results for the natural convection from a vertical flat plate are obtained and compared with the corresponding results documented in the literature to validate our results. Figure 2 shows the obtained axial velocity distribution by the present study and that presented by Schlichting [10]. Also, to verify the obtained results of the parabolic body cases, our code is modified to solve the governing equations considered by Haddad et al. [7] for the forced convection flow case. The local skin friction distribution along the body surface is shown in Fig. 3 for two different values of the Reynolds number (note: the Reynolds number is defined only for the forced convection flow case and is required here only to compare our results with Haddad et al. [7]). It is obvious from Figs. 2 and 3 that the results obtained by this study are in excellent agreement with those previously documented in the literature. This agreement has strengthened our confidence in the results and enabled us to move forward to the desired flow cases in the present study.

4.2. Velocity Distributions

The local velocity profiles for the four different cases of the nose radius of curvature under study are shown in Fig. 4. From this figure it is obvious that as the nose radius of curvature of the parabolic body (r) increases, the hydrodynamic boundary layer thickness increases. This is due to the increased gradient of the streamlines close to the body surface due to the increased body thickness with r, which then leads to an increased velocity component in the wall normal direction and hence a higher viscous diffusion rate. It is also noted that the peak of the velocity profiles shifts slightly away from the wall as r increases. This may also be attributed to the same mechanism explained above. Finally, it can be noted that the increase in the local velocity is not uniform as the nose radius of curvature (r) increases. This is more obvious near the leading edge region (Fig. 4a) than farther downstream, and it indicates the nonlinear effect of the nose radius of curvature on the hydrodynamics of the flow. A similar trend will also be observed in the thermal part of the results.

The effect of the Grashof number (Gr_x) on the axial velocity can be noted in the same figure discussed above. The change in the Grashof

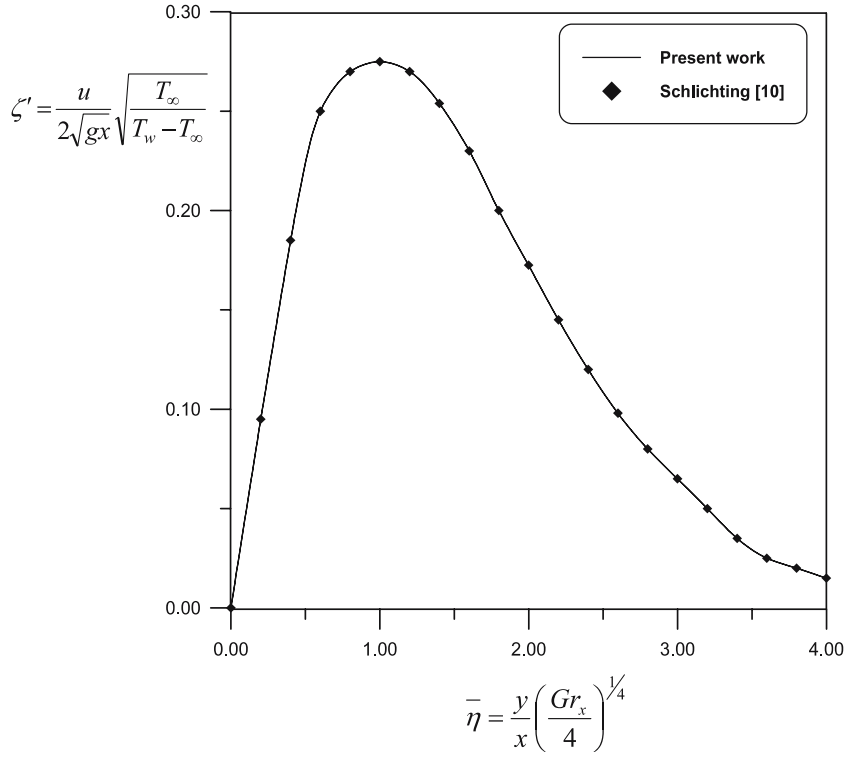

Fig. 2. Velocity distribution on a flat plate ($r = 0$).

number (which can be due to the change in the location along the body surface) affects the flow in a way such that as the Grashof number increases (as the flow travels farther down stream from x_1 to x_4) the axial velocity becomes relatively larger. This is due to the fact that the viscous boundary layer thickness becomes thicker as the fluid particles travel farther downstream; however, the continuity equation has to be satisfied everywhere.

Based on Fig. 4, it is also clear that the effect of bluntness (finite thickness leading edge) could be negligible only to some extent. In other words, the results of the flow over a parabolic body with $r = 0.001$ (finite thickness flat plate) are fairly close to the results when $r = 0$ (zero-thickness flat plate). However, the results of the other cases deviate significantly from the $r = 0$ case. Thus, up to $r = 0.001$, one may in general approximate finite thickness plates by zero-thickness plates and the effect of bluntness could then be considered negligible.

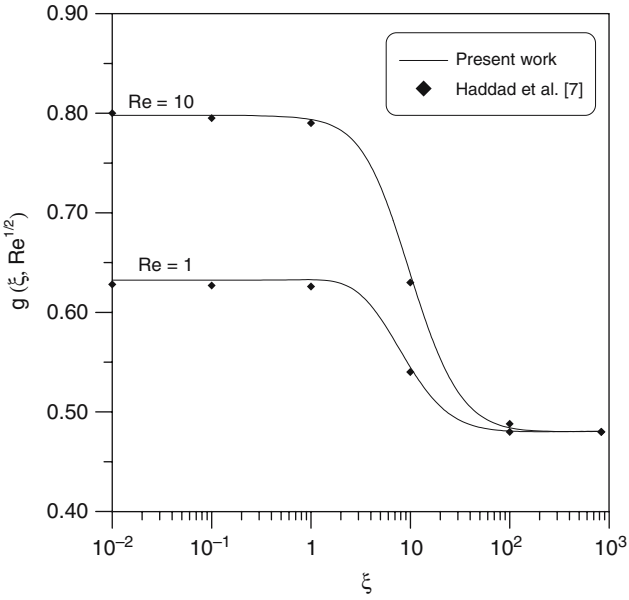

Fig. 3. Local skin friction distribution on parabolic bodies— forced convection.

The effect of fluid type on the results is manifested by changing the value of the Prandtl number. Figure 5 shows the effect of the Prandtl number on the velocity distribution at $x = x_1$ for a parabolic body of nose radius of curvature $r = 0.001$. It can be seen that as the Prantdl number increases, the axial velocity decreases. This is reasonable based on our knowledge that as Pr increases the flow becomes more viscous (i.e., the fluid's resistance to flow increases). Also, one may note that generally the flow velocity is relatively negligible for cases with $\mathrm{Pr} \geq 100$.

4.3. Temperature Distributions

4.3.1. Effect of the Nose Radius of Curvature (r) and the Fluid Type (Pr)

The dimensionless temperature profile is plotted for different values of the nose radius of curvature (r) at two different locations on the body. The results are shown in Fig. 6. It can be noted that as the nose radius of curvature increases, the thermal boundary layer thickness increases. This trend is present at all locations on the isothermal body, and this may be explained as follows: as the nose radius of curvature increases, the body becomes more blunt. This leads to an increased curvature in

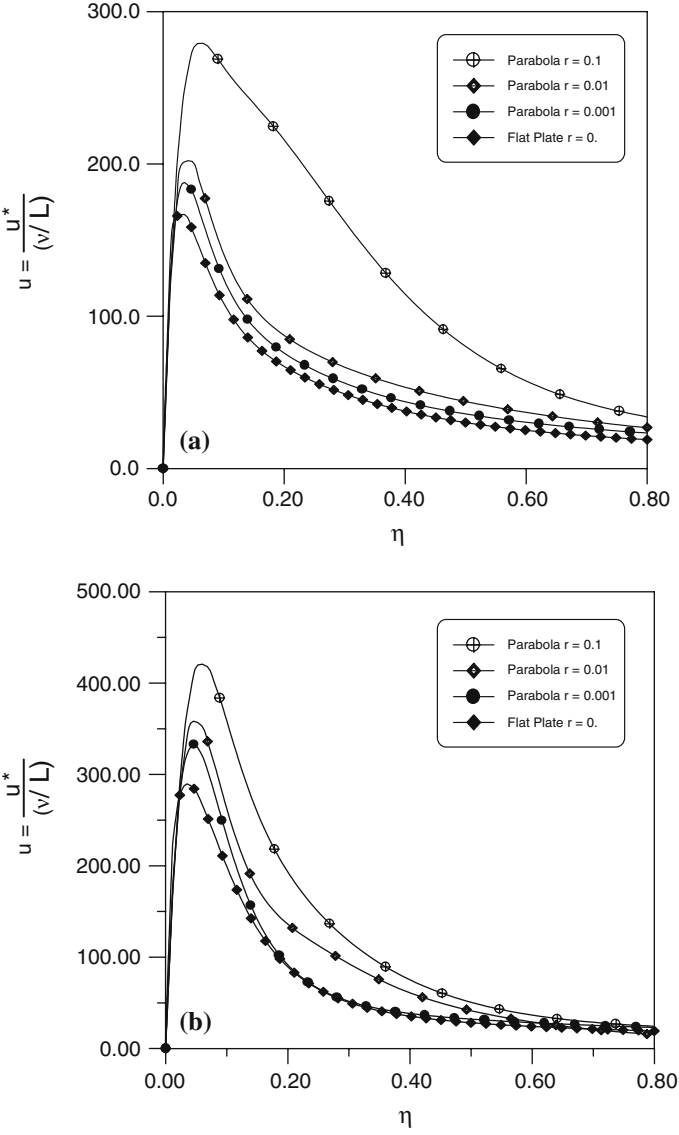

Fig. 4. Axial velocity distribution, $\mathrm{Pr} = 0.71$: (a) $x = x_1$ and (b) $x = x_4$.

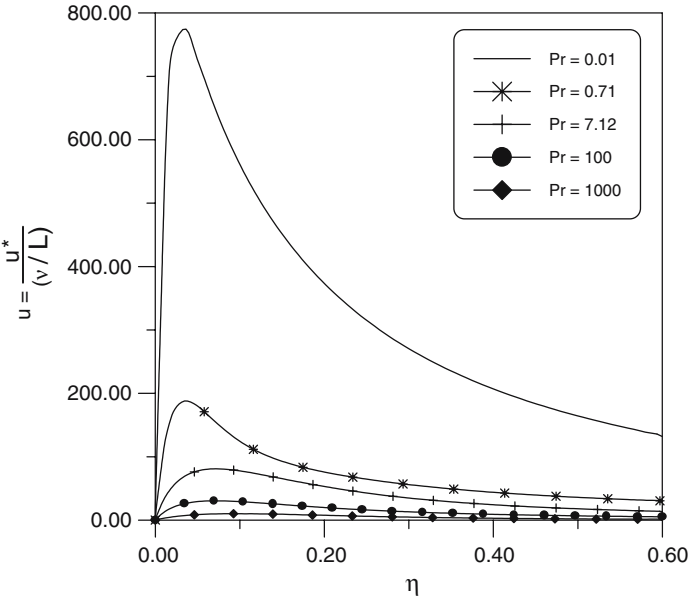

Fig. 5. Effect of Prandtl number on local velocity profile: $r = 0.001$, $x = x_1$.

the streamlines, which in turn increases the transverse component of the velocity vector. As a result, the flow penetrates farther in the wall normal direction and this leads to an increased thermal boundary layer thickness. It can also be noted that for values of the nose radius of curvature $r \leq 0.01$, the temperature distributions are close to the flat-plate solution. However, for $r = 0.1$ the distributions deviate clearly from the flat plate case. This deviation is vanishing with downstream distance. This indicates the importance of the leading edge region and confirms the fact that the flow approaches asymptotically the flat-plate (Blasius) flow far downstream (Davis [5]).

If the above results are interpreted in terms of the rate of heat transfer, it can be noted that as the nose radius of curvature is increased, the thermal boundary layer thickness will increase. This implies a lower temperature gradient at the wall which leads to a decreased rate of heat transfer at the surface. This result will be confirmed later by the Nusselt number distributions.

The effect of the Prandtl number on the temperature profiles is shown in Fig. 7. By inspecting Fig. 7, it should be noted that as the Prandtl number is increased the thermal boundary layer thickness is decreased. Consequently, an increased rate of heat transfer is expected as Pr is increased.

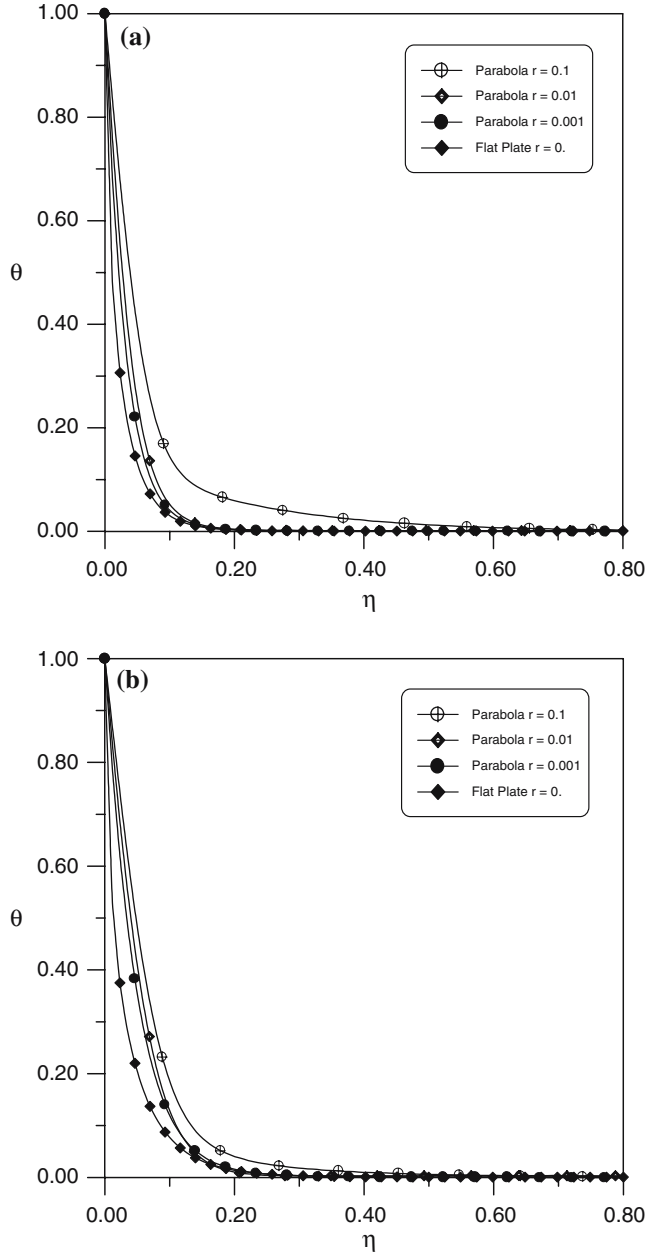

Fig. 6. Dimensionless temperature distribution: (a) $x = x_1$ and (b) $x = x_4$.

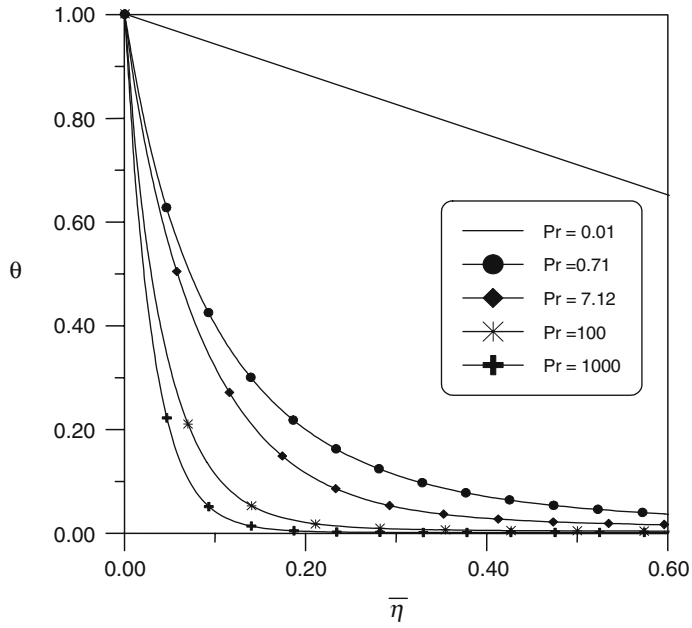

Fig. 7. Effect of Prandtl number on the dimensionless temperature distribution: $r = 0.001$, $x = x_1$.

4.3.2. Effect of Nose Radius of Curvature and Prandtl Number on Local and Average Nusselt Number Distributions

The local Nusselt number distribution along the body surface of different parabolic bodies and for two values of the Prandtl number, namely 0.71 (air) and 7.12 (water) is shown in Fig. 8. From this figure one may note the following:

(a) The local Nusselt number is maximum at the leading edge of the body and this, in part, can be attributed to the fact that in the vicinity of the leading edge the flow is a localized accelerating stagnation point flow (Davis [5]), and that is expected to enhance the mixing action locally and thus the local heat transfer rate is enhanced. Also, the local Nusselt number decreases asymptotically with downstream distance, as expected.

(b) The local Nusselt number decreases as the nose radius of curvature of the parabolic body increases: this is because as the nose radius of curvature of the parabolic body increases the thermal boundary layer thickness increases. This will decrease the

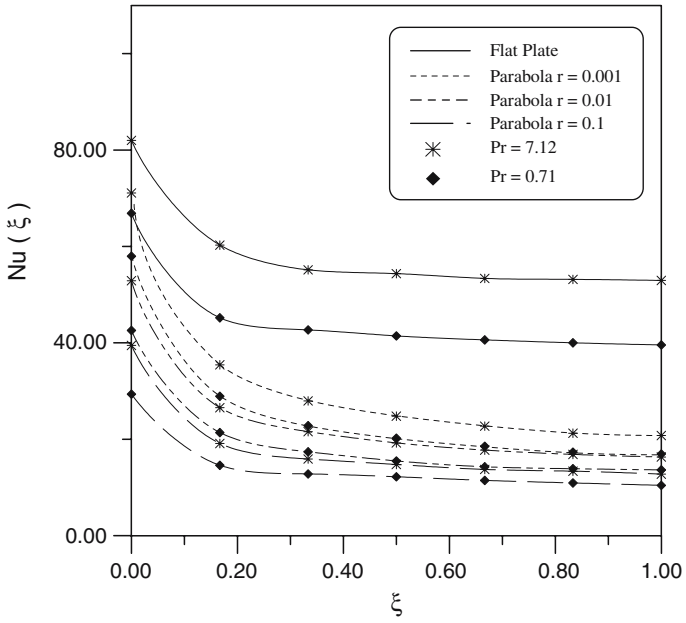

Fig. 8. Local Nusselt number distributions on parabolic bodies.

temperature gradient at the wall for a given driving temperature difference $(T_w - T_\infty)$ which in turn leads to a decreased value for the local Nusselt number. On the other hand, the trend of the local Nusselt number distribution over parabolic surfaces is similar to that over a flat plate.

(c) It should be noted that as the Prandtl number increases, the local Nusselt number (with all other conditions the same) increases. This trend may be explained as follows: the Prandtl number is the ratio of the viscous to thermal resistance, and as the Prandtl number increases the thermal resistance decreases, so the local Nusselt number will increase as stated above. The increase in the local Nusselt number is expected to enhance the local heat transfer rate.

The average Nusselt number profiles are shown in Fig. 9. In this figure one can note that the average Nusselt number (which reflects the overall heat transfer rate) increases linearly as the product (PrGr) increases. This is true for the flat plate and all parabolic bodies under consideration, as well. This trend may be discussed as follows: The increase in GrPr is related to the increase in one or both of Gr and Pr. The increase

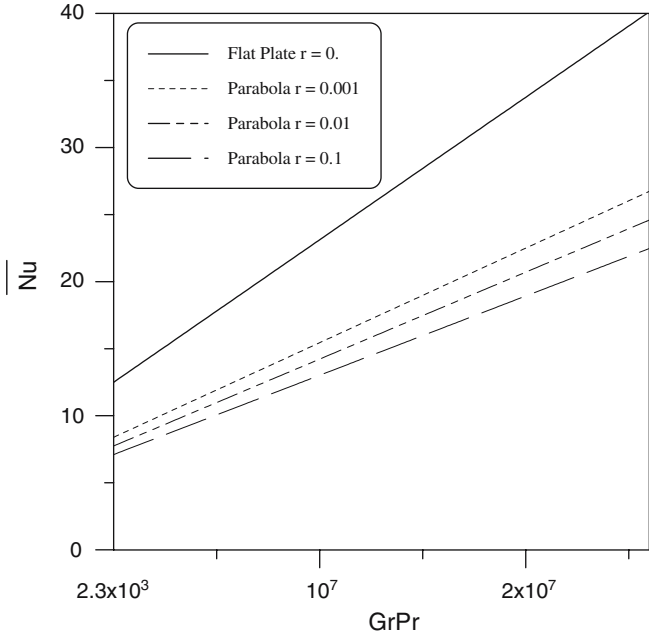

Fig. 9. Average Nusselt number distributions on parabolic bodies.

in Pr has been discussed above, while the increase in Gr will lead to an increase in the buoyancy force. This, in turn, increases the driving force and thus leads to a better heat transfer rate. Also, it should be noted that as the nose radius of curvature of the parabolic body increases, the average Nusselt number decreases (with all other boundary conditions the same). Recall that an increase in the nose radius of curvature results in a decrease in the local Nusselt number. Thus, it is expected that this decrease will be reflected on the average Nusselt number. This result is confirmed by Fig. 9.

In an attempt to correlate ($\overline{\mathrm{Nu}}$) to GrPr, the obtained results are curve fitted using the least-squares principle (i.e., regression analysis). The following results are obtained based on the data in Fig. 9:

1. Flat plate ($r = 0$):

$$\overline{\mathrm{Nu}} = 0.5529\,(\mathrm{Gr\,Pr})^{0.2487}.$$

This relation is in excellent agreement with that available in the literature (Schlichting [10]):

$$\overline{\mathrm{Nu}} = 0.5555\,(\mathrm{Gr\,Pr})^{1/4}.$$

2. Parabolic body ($r \neq 0$): using a similar form of the fitted equation to the one above, the following results are obtained for the cases when $r \neq 0$:

$$\overline{\mathrm{Nu}} = 0.3819\ (\mathrm{Gr}\,\mathrm{Pr})^{0.2467} \qquad r = 0.001$$

$$\overline{\mathrm{Nu}} = 0.3649\ (\mathrm{Gr}\,\mathrm{Pr})^{0.244} \qquad r = 0.01$$

$$\overline{\mathrm{Nu}} = 0.3529\ (\mathrm{Gr}\,\mathrm{Pr})^{0.2403} \qquad r = 0.1$$

These correlations provide accurate predictions of the Nusselt number for design and research purposes.

5. CONCLUSIONS

The hydrodynamic and thermal characteristics for laminar natural convection over parabolic bodies were investigated. A computer code based on a finite element method was developed to solve the flow problem under consideration. Results for the parabolic body and the flat plate (which is a special case of the parabolic body) are compared and discussed.

Some of the important conclusions that can be drawn from this study are as follows:

(a) Our results for both the hydrodynamic and thermal parts of the problem show excellent agreement with those available in the literature.

(b) For natural convection flow over a parabolic body, as the nose radius of curvature (r) increases, the thermal and viscous boundary layers become thicker and thus the local Nusselt number decreases (i.e., a decreased rate of heat transfer). Also, the peak of the velocity profiles shifts slightly away from the wall as r increases.

(c) The effect of bluntness (finite thickness leading edge) could be negligible only to some extent, that is, up to $r = 0.001$, one may in general approximate finite thickness plates by zero-thickness plates and the effect of bluntness could then be considered negligible.

(d) As the Grashof number increases, the axial velocity becomes relatively larger. On the other hand, as the Prandtl number increases, the flow velocity decreases, while the heat transfer rate will be enhanced.

NOMENCLATURE

A_{ij}	algebraic coefficient
g	acceleration of gravity
$\mathrm{Gr_x}$	local Grashof number ($g\beta\Delta T x^3/\nu^2$)
h	local convective heat transfer coefficient
k	thermal conductivity of the fluid
L	length of the parabolic body (x_6)
$\mathrm{Nu_x}$	local Nusselt number (hx/k)
$\overline{\mathrm{Nu}}$	average Nusselt number
Pr	Prandtl number (ν/α)
R	nose radius of curvature
r	dimensionless nose radius of curvature (R/L)
Re	Reynolds number based on the nose radius of curvature ($u_\infty R/\upsilon$)
S_t	source term
T	temperature
u	axial velocity component
v	normal velocity component
x, y	Cartesian coordinates

Greek Symbols

(ξ, η)	body fitted (i.e., parabolic) coordinates ($x=(\xi^2-\eta^2)/2$, $y=\xi\eta$)
$\overline{\eta}$	modified wall normal coordinate, $\overline{\eta}=\frac{y}{x}\left(\frac{\mathrm{Gr}_x}{4}\right)^{1/4}$
μ	dynamic viscosity
υ	kinematic viscosity
ρ	density
θ	dimensionless temperature
γ	under-relaxation coefficient
ϕ	arbitrary dependent variable
α	thermal diffusivity

Superscripts

$*$	dimensional quantity
—	average quantity

REFERENCES

1. R. T. Davis, *J. Fluid Mech.* **27**:691 (1967).
2. A. I. Van De Vooren and D. Dijkstra, *J. Eng. Math.* **4**:9 (1970).

3. E. F. F. Botta, D. Dijkstra, and A. E. P. Veldman, *J. Fluid Mech.* **6**:63 (1972).
4. S. C. R. Dennis and J. D. Walsh, *J. Fluid Mech.* **50**:801 (1971).
5. R. T. Davis, *J. Fluid Mech.* **51**:417 (1972).
6. O. M. Haddad and T. C. Corke, *J. Fluid Mech.* **368**:1 (1998).
7. O. M. Haddad, M. Abu-Qudais, and A. M. Maqableh, *Int. J. Numer. Methods Heat Fluid Flow* **10**:80 (2000).
8. S. V. Patanker, *Numerical Heat Transfer and Fluid Flow* (Hemisphere, New York, 1980).
9. D. A. Anderson, J. C. Tannehill, and R. H. Pletcher, *Computational Fluid Mechanics and Heat Transfer*. (Hemisphere, New York, 1984).
10. H. Schlichting, *Boundary Layer Theory*, 7th edn., translated by J. Kestin (McGraw-Hill, New York, 1979).